Title:

A neonatal mouse model characterizes transmissibility of SARS-CoV-2 variants and reveals a role for ORF8

Authors: Bruno A. Rodriguez-Rodriguez[1], Grace O. Ciabattoni[1], Ana M. Valero-Jimenez[1], Keaton M. Crosse[1], Austin R. Schinlever[1], Joaquin J. Rodriguez Galvan[1], Ralf Duerr[1], Stephen T. Yeung[1], Marisa E. McGrath[2], Cynthia Loomis[3], Kamal M. Khanna[1,4], Ludovic Desvignes[5,6], Matthew F. Frieman[2], Mila B Ortigoza[1,5]*, and Meike Dittmann[1]*

Affiliations: [1]Department of Microbiology, New York University Grossman School of Medicine, New York, New York, USA

[2]Department of Microbiology and Immunology, Center for Pathogen Research, University of Maryland School of Medicine, Baltimore, MD 21201

[3]Department of Pathology, New York University School of Medicine, New York, New York, USA

[4]Perlmutter Cancer Center, New York University Langone Health, New York, NY, USA

[5]Department of Medicine/Division of Infectious Diseases and Immunology, New York University Grossman School of Medicine, New York, New York, USA

[6]High Containment Laboratories - Office of Science and Research, NYU Langone Health, New York, New York, USA

*Co-corresponding authors

Summary paragraph

Small animal models have been a challenge for the study of SARS-CoV-2 transmission, with most investigators using golden hamsters or ferrets [1,2]. Mice have the advantages of low cost, wide availability, less regulatory and husbandry challenges, and the existence of a versatile reagent and genetic toolbox. However, adult mice do not transmit SARS-CoV-2 [3] . Here we establish a model based on neonatal mice that allows for transmission of clinical SARS-CoV-2 isolates. We characterize tropism, respiratory tract replication and transmission of ancestral WA-1 compared to variants alpha (B.1.1.7), beta (B.1.351), gamma (P.1), delta (B.1.617.2) and omicron (B.1.1.529). We identify inter-variant differences in timing and magnitude of infectious particle shedding from index mice, both of which shape transmission to contact mice. Furthermore, we characterize two recombinant SARS-CoV-2 lacking either the ORF6 or ORF8 host antagonists. The removal of ORF8 shifts viral replication towards the lower respiratory tract, resulting in significantly delayed and reduced transmission. Our results demonstrate the potential of our neonatal mouse model to characterize viral and host determinants of SARS-CoV-2 transmission, while revealing for the first time a role for an accessory protein this context.

Introduction

Despite worldwide vaccination efforts and increasing natural immunity, emerging SARS-CoV-2 variants continue to infect and burden the health of millions of people[4]. Past variants of concern include alpha (B.1.1.7), beta (B.1.351), gamma (P.1), delta (B.1.617.2) and omicron (B.1.1.529), while omicron sub-lineages BA.4.6, BA.2.75 and BF.7 currently dominate the second half of 2022 [5]. Variants differ in key genes across the viral genome, including Spike (*S*), *ORF1a*, *ORF1b*, Nucleocapsid (*N*), *ORF3a*, *ORF6*, *ORF7a*, *ORF8*, *ORF9b*, Envelope (*E*), and Membrane (*M*). Much attention has been given to changes in Spike, as this envelope glycoprotein is the antigen targeted for most vaccination strategies to date and is key to viral entry into cells [6]. Other key hotspots that accumulate mutations in SARS-CoV-2 variants are accessory proteins, of which SARS-CoV-2 encodes 8, and some serve as antagonists of the antiviral host response, most notably type I interferon production and response[7-13]. Our knowledge of SARS-CoV-2 ORFs stems from inferring functional similarities of well-studied antagonists encoded by SARS-CoV and other coronaviruses, and from limited functional studies using SARS-CoV-2 ORF cDNA overexpression constructs or recombinant SARS-CoV-2 [9,11,12,14]. The high number of SARS-CoV-2 infections coinciding with the appearance of new variants raised concerns about enhanced transmission of these variants, posing considerable ramifications for resolution of the COVID-19 pandemic [15].

Molecular characterization of SARS-CoV-2 variants is essential to our ability to develop appropriate antiviral strategies. Previous studies have characterized SARS-CoV-2 variants *in vitro* by evaluating receptor binding and affinity, antigenic escape and replication dynamics[16-22] as well as *in vivo* regarding pathogenesis and immune evasion[16,23-37]. However, comparative studies on variant transmission and the molecular mechanisms governing transmission differences as a result of variant-specific mutations are still scarce, mainly due to limitations inherent to current animal models. These models include ferrets and hamsters, which are excellent models for pathogenesis. Ferrets display high upper respiratory tract (URT) shedding, resulting in robust

contact transmission but minimal aerosol transmission. Hamsters display a high but short peak of viral shedding, leaving a small window for transmission to occur [2,38]. Despite this, both contact and aerosol transmission in most experimental hamster scenarios is 100% effective, which complicates the assessment increased transmission [2]. Both the ferret and the hamster model require special husbandry environments, and the lack of species-specific reagents is limiting. Although hamsters can undergo genetic manipulation to address host determinants of transmission [39], the process involves several complicated steps that result in limited availability of transgenic hamster lines. In contrast, mice offer a versatile and readily available genetic toolbox, and reagents are widely available; however, adult mice do not readily transmit respiratory viruses such as SARS-CoV-2 or influenza virus, a problem that has long stymied the field [3]. To overcome this hurdle, we previously established a model for influenza virus transmission using neonatal mice of 4-7 days of age [40]. In contrast to adult mice, the success of intra-litter virus transmission between pups is likely due to their 1) Relative immune immaturity/tolerance towards infections, 2) Reduced mobility, which increases contact between pups and/or 3) Increased secretions during feeding by suckling. The mode of transmission in this model is a combination of direct contact and droplet transmission and, to a lesser extent, indirect contact (fomite) and aerosol transmission [40]. Although it has been successfully applied to study molecular mechanisms of influenza A virus transmission, the model is not established for other respiratory viruses, such as SARS-CoV-2.

Here, we present a neonate K18-hACE2 mouse model that allows for transmission of SARS-CoV-2 between pups of the same litter, and we examine side-by-side the transmission of early and current SARS-CoV-2 variants of concern (VOC). In addition, we characterize the transmission of two recombinant SARS-CoV-2, lacking accessory proteins ORF6 or ORF8. Our study showcases the power of our model to elucidate the dynamics of SARS-CoV-2 variant transmission and provides evidence of an accessory protein, ORF8, to be critical for SARS-CoV-2 transmission. Our tractable small animal model will help decipher some of the most decisive aspects of SARS-CoV-2 continued spread in the human population.

Results

Neonatal K18-hACE2 mice efficiently support SARS-CoV-2 WA-1 transmission

While influenza viruses readily infect wild-type mice, the ancestral SARS-CoV-2 and the clinically important delta variant rely on the human version of the SARS-CoV-2 host cell receptor, ACE2, and cannot engage murine Ace2 [22]. In contrast, a number of other SARS-CoV-2 variants acquired specific Spike mutations, most notably N501Y, which allows them to bind murine Ace2 [41]. Ultimately, we aimed to use our model to compare a panel of variants, from alpha to omicron, to the ancestral SARS-CoV-2. With this in mind, we developed our neonate model using K18-hACE2 mice, which express human ACE2 under the control of the K18 promoter [42].

We combined C57BL/6 K18-hACE2$^{+/+}$ males and C57BL/6 (hACE2$^{-/-}$) females to produce SARS-CoV-2 WA-1 permissive K18-hACE2$^{+/-}$ offspring. At 4-7 days of age, index pups were infected intranasally with 3 µL of ancestral SARS-CoV-2 USA_WA-1/2020 (WA-1) without anesthesia and placed back with the (non-permissive) dam and their (permissive) naïve littermates to allow for intra-litter transmission (**Fig 1a**). A previous dose-response experiment revealed that 30 PFU of WA-1, as determined by plaque assay on VeroE6 cells, was the minimum dose to yield robust index infection (**Extended data Fig 1a**). We monitored the pup's weight and survival daily and collected longitudinal shedding samples non-invasively, and without anesthesia (**Fig 1a**). Thus, we were able to leverage the kinetics of upper respiratory tract (URT) shedding as a measure of viral infection.

We used the lack of weight gain as a proxy for morbidity. Index pups failed to gain further weight by day 3 post-infection (3 dpi), and they all succumbed to infection by 4 dpi (**Fig 1b, 1c**). Morbidity and mortality were offset in contact mice by 2-3 days compared to index mice, which was the first indication of successful transmission. In index mice, we detected SARS-CoV-2 RNA as early as 1 dpi, whereas contact pups began shedding viral RNA from 2 dpi (**Fig 1d**). A parallel

experiment with heat-inactivated SARS-CoV-2 showed that the viral genomes in shedding samples were due to active viral replication and not carryover from inoculates (**Extended data Fig 1b**). Detecting SARS-CoV-2 RNA in contact mice was thus another indication of transmission. However, we stringently define transmission as the detection of infectious viral particles in contact mice. Therefore, we next determined viral titers in nasal shedding samples by plaque assay. Infectious particles from index mice (**Fig 1e**) correlated with the onset of RNA detection (**Fig 1d**) but decreased by day 3, contrasting ongoing elevated RNA levels. Detection of infectious particles in contact pups confirmed viral transmission (**Fig 1e**). Infectious particles in contacts peaked on day 4 and decreased by days 5 and 6, whereas viral RNA remained elevated. Of note, all contact pups shed infectious particles by day 4, representing 100% transmission efficiency of WA-1 in our model.

Detection of infectious particles in shedding samples of K18-hACE2 neonatal mice suggested robust viral infection in the URT. To determine the sites of infection within the URT, we performed immunohistochemistry on the nasopharynx of index pups. Heads of neonatal mice were harvested at their peak of viral shedding (2 dpi), sectioned through the nasopharynx, and stained for SARS-CoV-2 N protein. We detected SARS-CoV-2-positive cells in the upper olfactory and respiratory epithelium lining, demonstrating replication of SARS-CoV-2 WA-1 in cells of the URT (**Fig 1f**). Taken together, these results establish and validate a tractable neonatal K18-hACE2 mouse model for the transmission of SARS-CoV-2.

SARS-CoV-2 variants of concern display distinct replication dynamics and tropism in neonatal index mice

The high transmissibility of a number of SARS-CoV-2 variants, namely alpha and delta, has been proposed to be linked to their success in efficient URT replication [34,43,44]. To characterize SARS-CoV-2 variant replication dynamics, we first generated clonal (plaque-purified), sucrose-purified, and deep-sequenced viral working stocks. This rigorous quality-control pipeline ensures

the identity of VOCs, the lack of tissue culture-induced mutations, and the purity of inoculates (i.e. the lack of cell debris or cytokines from producer cell supernatants). We infected K18-hACE2$^{+/-}$ index mice with 30 PFU of either SARS-CoV-2 WA-1, B.1.1.7 (alpha), B.1.1.351 (beta), P.1 (gamma), B.1.617.2 (delta) or B.1.1.529 (henceforth referred to as omicron BA.1). We first determined the peak day of viral shedding for each isolate (**Fig 2a**). Shedding from mice infected with ancestral WA-1, beta, gamma, and delta peaked at 2 dpi, before decreasing by 3dpi. (**Fig 2b,2e-g**) In contrast, alpha peaked earlier, at 1 dpi, and steeply decreased almost 1000-fold by 2 dpi (**Fig 2d**), which may indicate reduced stability of this variant. Notably, mice infected with omicron expelled low levels of virus, with most replicates below the detection limit and just one replicate at 2 x 10^3 PFU/mL at 1 dpi (**Fig 2h**).

To characterize the sites of viral replication for each variant, we next measured infectious particles in shedding samples (representing expelled virus), in retrotracheal lavages (representing virus present in the upper respiratory tract), and in lung homogenates (representing virus present in the lower respiratory tract). We collected these samples at the respective first peak day of shedding (2 dpi for WA-1, beta, gamma, and delta; 1 dpi for alpha and omicron), and quantified the amount of infectious virus particles by plaque assay (**Fig 2c, 2i-2m**). We found the distribution of viral load in these sample types to be distinct for specific viruses. For ancestral WA-1, expelled and URT titers were both an average of 10^5 PFU/mL, while titers in the lungs were significantly higher (5x10^6 PFU/mL) (**Fig 2c**). For alpha, expelled and URT titers were comparable in magnitude to WA-1, but lung titers were significantly lower (**Fig 2i**). This suggests that in our model, at peak shedding day, alpha replication favors the URT – this may be different on following days and as the infection progresses from the URT to the lungs. For beta, gamma, and delta we found no significant differences in titers between expelled virus, URT, and lungs, suggesting equal ability to infect and replicate in both the URT and the lower respiratory tract and to be expelled from the URT (**Fig 2j, 2k, 2l**). Indeed, immunohistochemistry of the URT region confirmed that WA-1, alpha, beta, gamma and delta infect the URT efficiently (**Fig 1f and Fig 2n**). In contrast,

omicron titers in the URT were low (**Fig 2m**), and immunohistochemistry did not reveal omicron-infected cells in the URT epithelium. No infectious omicron particles were detected in the lungs, suggesting that this variant might not replicate efficiently in neonatal K18-hACE2 mice. Our results are in line with findings from others, showing that the omicron BA.1 variant is attenuated in mice and hamsters [23,30,37]. Of note, viral loads in shedding samples were similar to those from their respective retrotracheal lavage samples, showing that 1. viruses assayed do not seem to have a defect in viral expulsion and that 2. in this model, URT shedding can be used as a proxy for URT replication.

Taken together, our results demonstrate that, except for omicron, our model allows for efficient replication and shedding of different SARS-CoV-2 VOCs at comparable levels to the ancestral WA-1. Temporal shedding dynamics differ between variants, which we hypothesize is a result of the differences in viral stability, and allows this model to be used as a tool to understand the mechanisms of variant SARS-CoV-2 transmission.

Neonatal mouse model reveals dynamics in SARS-CoV-2 variant transmission

We next utilized our panel of SARS-CoV-2 variants ranging from early to current pandemic isolates to test transmission. We infected 4-7-day-old index K18-hACE2$^{+/-}$ mice with either ancestral SARS-CoV-2 WA-1, alpha, beta, gamma, delta or omicron BA.1 and cohoused them with naïve neonatal mice at a 1:6-9 ratio.

In index mice, morbidity (lack of weight gain) and mortality occurred earlier in mice infected with WA-1, alpha, or beta than in mice infected with delta or gamma (**Extended Data Fig 2a-2e**). Index mice infected with omicron BA.1 displayed delayed morbidity and succumbed to infection (**Extended Data Fig 2f**). Except for omicron some or all contact mice in cages with other variants succumbed to infection by 7 dpi, suggesting transmission for these variants (**Extended data Fig 2**). The acquired morbidity and mortality by the naïve contacts indicated that our model captured

differences in SARS-CoV-2 variant transmission, which led us to investigate the dynamics of viral shedding in the index and contact mice.

To capture the kinetics and dynamics of variant transmission, we next analyzed URT shedding samples in contact pups. Both ancestral WA-1 and alpha infectious particles were detected in contact mice as early as 1 dpi. Alpha URT titers peaked at 4 dpi, and faded earlier than WA-1, starting at 4 dpi, (**Fig 3a**), which is in line with the early drop of infectious titer previously observed in index mice (**Fig. 2d**). We next used infectious particle URT shedding from contact mice as a proxy for successful viral acquisition and replication, and found that alpha showed similar transmission dynamics to WA-1 (**Fig 3a**). In contrast, beta displayed later onset of particle shedding from contacts than WA-1, at 2 dpi, but reached similar magnitude (**Fig 3b**). However, the viral acquisition dynamics were significantly different from WA-1, lagging on average by 1 day. Gamma showed significantly later onset of infectious particle detection in contacts compared to WA-1, and had overall lower viral load, although the slope of infectious particle onset and waning was similar to that of WA-1 (**Fig 3c**). In addition, gamma showed significantly delayed acquisition compared to WA-1. Delta lagged 1 day regarding onset of shedding from contacts, similar to gamma, but then reached similar infectious virus levels as WA-1 (**Fig 3d**). Interestingly, delta-infected contacts kept shedding infectious particles until the end of the experiment at 7 dpi. Viral acquisition of delta was significantly delayed compared to WA-1. Finally, omicron did not transmit (**Fig 3e**). This result is similar to observations for omicron transmission in the hamster model (personal communication by Yoshi Kawaoka, Jacco Boon, and other NIAID SAVE investigators).

We next defined the minimum index shedding threshold required for productive SARS-CoV-2 transmission in our model (**Fig. 3f**). The threshold is equal to or above 1.2 x 10^4 PFU/mL, which was the lowest titer obtained at the peak shedding day among WA-1, alpha, beta, gamma, and delta variants. Using omicron as a non-transmitter, we define that index shedding titers at or below 2.7 x 10^3 PFU/mL would likely not allow for transmission in our model. While these

thresholds may allow for a prediction of a variant's transmission potential based on index mice shedding, it is important to note that in experimental conditions with additional transmission bottlenecks, such as adaptive immune status of the index and/or contact mice, the thresholds are likely different.

An antiviral/inflammatory response to infection is expected to attenuate the virus within the host, causing reduced transmission [45,46]. However, increased inflammation may also induce URT secretions that help expel the virus into the environment, which may favor transmission [47,48]. In order to link a variant's URT inflammatory repertoire with its transmission potential, we analyzed the cytokines present in the URT shedding samples of neonatal mice. We first validated our system with either heat-inactivated (HI) SARS-CoV-2 WA-1 or poly (I:C). We detected a higher overall cytokine signature in shedding samples from animals treated with poly (I:C), validating the detection of cytokine responses in our model (**Extended Data Fig 3a**). We next measured cytokines in shedding samples in neonatal mice infected with either HI SARS-CoV-2, SARS-CoV-2 WA-1 or SARS-CoV-2 variants alpha, beta, gamma, delta, and omicron. (**Extended Data Fig 3b**). We chose samples with comparable viral titers, between 10^4 and 10^5 PFU/mL, except for omicron BA.1, which was 10^1 PFU/mL, allowing for qualitative comparison of cytokine signatures between equally replicating viruses. Indeed, the cytokine signature for omicron was most similar to that of HI SARS-CoV-2 (**Extended Data Fig 3b**), likely reflecting the poor replication of omicron BA.1 in our model (**Fig 2h, 2m, 3f**). For equally replicating viruses WA-1, alpha, beta, gamma, and delta we found that cytokine signatures did not generally correlate with their transmission dynamics. For example, WA-1, beta, and gamma infections, whose transmission differed in terms of onset, slope of viral shedding, and slope of acquisition, resulted in overall similar cytokine responses (**Extended Data Fig 3b**).

Taken together, our results show that, except for omicron BA.1, our neonatal mouse model is able to reveal the transmission dynamics inherent to the SARS-CoV-2 variants. Our non-invasive method of viral sampling enables tracking viral replication in individual index and contact

mice over time, providing unprecedented granularity in transmission parameters, including the characterization of variant-specific cytokine signatures.

Accessory proteins ORF6 and ORF8 play a role in successful SARS-CoV-2 transmission

In addition to mutations in spike, a number of SARS-CoV-2 variants display mutations in accessory genes, such as *ORF3*, *ORF6*, *ORF7*, and *ORF8*, which have been implicated in the interference of immune signaling or direct host effector counteraction [9,35]. The selective advantage of changes in these accessory proteins remains largely undefined, particularly regarding transmission. We thus aimed to determine how the lack of specific accessory proteins impacts SARS-CoV-2 transmission in our model, and focused on two accessory proteins: ORF8, because it has mutations defining the alpha, gamma, and delta variants, and, ORF6, which lacks mutations in the variants utilized in this study but is mutated in other omicron variants (BA.2, BA.2.12 and BA4) in addition to being one of the best-characterized SARS-CoV-2 accessory proteins [7,10,11,35,49].

We infected K18-hACE2$^{+/-}$ neonatal mice with 30 PFU_{VeroE6} of recombinant SARS-CoV-2 WA-1 (rWA-1), recombinant SARS-CoV-2 lacking ORF6 (ΔORF6), or recombinant SARS-CoV-2 lacking ORF8 (ΔORF8). Similar to our previous observations with the clinical WA-1 isolate (**Fig 2b**), shedding titers from index mice peaked at 2 dpi and decreased by 3 dpi (**Fig 4a**). Index shedding from WA-1 ΔORF6 infected mice was similar to WA-1 in both dynamic and magnitude (**Fig 4b**). In contrast, index mice infected with WA-1 ΔORF8 consistently shed up to 100-fold less virus than mice infected with WA-1 (**Fig 4c**), and survived longer than WA-1 infected mice (data not shown), hence still shedding at 4 dpi. Next, we observed a trend of higher recombinant SARS-CoV-2 WA-1 titers in the lungs, $5x10^5$ PFU/mL, and lower titers in the URT and shedding samples, at $1x10^5$ or $5x10^4$ PFU/mL, respectively (**Fig 4d**). For WA-1 ΔORF6, we obtained similar titers in all three sample types, $1x10^4$ PFU/mL on average, although there was a broad distribution with some pups displaying higher viral titers in the lung than in shedding or URT samples (**Fig 4e**). We concluded that, in our model, the lack of ORF6 did not attenuate viral replication or significantly

change tissue tropism with respect to parental WA-1. This was different for ORF8. WA-1 ΔORF8 expelled virus loads and URT virus loads were $5x10^2$ or $1x10^3$ PFU/mL, respectively, and thus lower than for WA-1 or WA-1 ΔORF6 (**Fig 4f**). In contrast, lower respiratory tract burden was comparable to those of WA-1 and WA-1 ΔORF6, an average of $5x10^4$ PFU/mL. Thus, the lack of ORF8 seems to significantly reduce WA-1 ΔORF8's ability to robustly replicate specifically in the URT. To our knowledge, this is the first report of ORF8's role in SARS-CoV-2 URT replication.

We next performed transmission experiments with the three recombinant viruses. Similar to the WA-1 isolate, recombinant WA-1 transmission first occurred at 1 dpi, was complete by 4 dpi, and contact shedding titers decreased from 4dpi onwards (**Fig 4g,4j**). WA-1 ΔORF6 was similar to parental WA-1 in both contact shedding onset, dynamics, and acquisition slope (**Fig 4h,4k**). Together, these results suggest that the lack of ORF6 does not negatively impact viral replication or transmission in our model. Onset of transmission for WA-1 ΔORF8 was similar to WA-1 and WA-1 ΔORF6, 1 dpi, (**Fig 4i**) but in contrast to the other two recombinant viruses, the slope of transmission was slower, and transmission remained incomplete until the experiment ended at 7 dpi (**Fig 4l**). We hypothesize that this reduction in transmission is a consequence of the low and declining viral loads expelled by the index mice. This is consistent with our initial observation that index mice shedding must surpass the transmission threshold of 2.7×10^3 PFU/mL in order to efficiently transmit virus to naïve contacts in this model.

Next, we analyzed the presence of COVID-19-associated inflammatory cytokines (IL-6, IL-1α, and IFN-β) in URT and lung samples from index mice infected with the three recombinant viruses at 2dpi (**Fig 4m-4o**). We found that inflammatory cytokines present in the URT of mice infected with WA-1 ΔORF8 had a similar magnitude to those infected with WA-1 and WA-1 ΔORF6, despite 100-fold lower WA-1 ΔORF8 titers at the same time point. This suggests increased relative inflammatory potential of WA-1 ΔORF8. In lungs, which display similar viral titers across the three viruses (**Fig 4d-4f**), we observed increased amounts of some inflammatory cytokines by WA-1 ΔORF8 (**Fig 4m, 4n and Extended Data Fig 4c, 4d,4f**), which has also been

reported in adult mice [35]. How and whether inflammation by WA-1 ΔORF8 attenuates viral replication specifically in the URT, but not in the lungs, remains the topic of further investigation. Taken together our results show how removal of one SARS-CoV-2 accessory protein, ORF8, reduces URT replication, resulting in reduced shedding and transmission.

Discussion

Mouse models of SARS-CoV-2 infection have been utilized extensively to study the pathogenesis of emerging SARS-CoV-2 variants [16,23,31,35,37,50-52]. However, adult mice do not readily transmit SARS-CoV-2 [3]. In our study, we developed and validated a neonatal mouse model to characterize the transmission of SARS-CoV-2 based on our previous experience with influenza A virus (Fig. 1, [40]). Using a unique SARS-CoV-2 panel spanning early to current pandemic isolates, we demonstrate how variant-inherent mutations affect tropism and shedding (Fig 2), transmission (Fig 3), and upper respiratory tract cytokine repertoires (Extended Data Fig 3). Finally, our study reveals a previously unappreciated role for the accessory protein ORF8 in viral upper respiratory tract replication and transmission (Fig 4), showcasing the power of our model to study the molecular determinants of SARS-CoV-2 transmission.

Our model has several advantages over existing animal models of SARS-CoV-2 transmission: First, amenability to a wide range of available knockout animals allows for systematic studies determining host factors that are critical for transmission. Second, our model allows for powered studies, as high numbers of contact neonatal mice are more easily achieved than in other animal models. Third, there are fewer husbandry challenges to work with mice as compared to hamsters or ferrets. Further, the availability of mouse-specific reagents and tools increases the potential to study virus-induced immune pathways in the host, as well as respiratory mechanics that could impact transmission, such as respiratory system resistance/elastance and inspiratory capacity. Next, our inoculation procedure without anesthesia, which initiates infection in the URT before progressing to the lower respiratory tract, is unique in SARS-CoV-2 research.

We argue that this route of infection may recapitulate SARS-CoV-2's natural infection route better than models using deep anesthesia, in which deep inhalation favors lower respiratory tract infection. Although inoculation with anesthesia has been shown to produce the typical lung pathology associated with COVID-19 in K18-hACE2 mice [50], this approach could have a significant impact on transmission as it mainly circumvents the initial URT infection. Finally, we are able to track the progression of the index and contact infection longitudinally, due to non-invasive sampling. This provides more granularity and insight into the kinetics of viral shedding and URT viral load at the level of individuals, which illuminates our understanding of transmission efficiency.

Although these features establish our model as a unique and workable tool for studying SARS-CoV-2 transmission, other animal models, such as hamsters and ferrets, have certain advantages over the limitations of our system. For instance, our transmission model is based on a mixture of droplet and contact transmission [40]; therefore, any variant-intrinsic differences that can be affected by airborne droplet formation and virion stability, cannot be studied in our system, as opposed to the hamster model [24,53]. An additional limitation of our model is the non-physiological expression of hACE2. The expression of the hACE2 transgene is driven by a non-native K18 promoter, allowing the infection of multiple organs and resulting in tissue expression levels that are distinct from endogenously expressed ACE2 [42,50]. Although the expression is non-physiological, we deliberately chose K18-hACE2 mice for this first study of SARS-CoV-2 transmission in mice since our goal was to investigate and compare transmission of early and current pandemic isolates, some of which are unable to engage murine Ace2. We recognize that extrapolating tropism changes in our model to tropism in humans warrants caution, especially if these changes are solely brought upon by changes in variant spike-ACE2 binding, i.e. through mutations in spike's receptor binding site. However, we argue that tropism changes brought upon by differences in spike processing and/or by differences in host-virus interplay can be readily interpreted using our model, since protease expression and inflammation or antagonism are

unadulterated by the hACE2 transgene. Taken together, our study demonstrates how the selection amongst available animal models should be based on research scope and context, as each of them can provide valuable and non-redundant information regarding SARS-CoV-2 biology.

In our system, except for omicron, we observed above 90% SARS-CoV-2 variant transmission, yet, our method was granular enough to detect subtle differences between variants. For example, we identified an early but narrow peak of URT replication for alpha, leaving only a short window for transmission. Despite this, contact animals acquire alpha at a similar rate to ancestral WA-1. In fact, alpha was the only virus with similar transmission fitness to WA-1, while all other variants displayed a significant delay in transmission compared to WA-1. Variants post-alpha arose after widespread population immunity brought by either prior infection or immunization, and viral evasion from neutralization due to mutations in the variants' spike gene is well-documented [5,21,54-56]. Thus, we speculate that transmission differences between WA-1 and variants beta to delta may have been less dramatic under adaptive immune pressure or even reveal a transmission advantage for these variants compared to the ancestral virus, to which most immunization regiments are currently matched. Future studies with this model will introduce adaptive immune pressures by vaccination of dams prior to pregnancy. Offspring will acquire immunoglobulins via transplacental passage or milk, which has been shown to reduce transmission in our influenza A virus model [40].

SARS-CoV-2's accessory protein ORF8 is arguably the most enigmatic, as it only shares a 20% protein identity with SARS-CoV. For SARS-CoV-2, ORF8 is a secreted glycoprotein, and diverse immunomodulatory functions have been proposed, such as IL-17A mimicry [57] and downregulation of MHC class I [58], although the full spectrum of ORF8's functions and mechanisms of action remain to be elucidated [59]. In our model, deletion of ORF8 resulted in reduced replication specifically in the URT. The magnitude of inflammatory cytokines (Fig 4) and inflammation (Extended Data Fig 4) we observe for ΔORF8 in the URT was similar to those of parental WA-1

or ΔORF6 virus, despite 100-fold less virus in that compartment. It is feasible that in the absence of ORF8, SARS-CoV-2 fails to suppress critical antiviral responses in the URT. We argue that the reduced URT replication is the cause of ΔORF8's delayed and reduced transmission. We further argue that this is not due to an overall attenuation of SARS-CoV-2 lacking ORF8, as these viruses replicate efficiently in the lungs of both neonatal and adult K18-hACE2 mice (Fig 4 and [35,60]). To our knowledge, this is the first report of a compartment-specific role of a SARS-CoV-2 accessory protein. Although underlying mechanisms for the URT-specific role of ORF8 remain unknown, it is possible that antiviral inflammatory processes brought upon by SARS-CoV-2 infection are different in the URT from those in the lower respiratory tract. For instance, the cellular milieu and temperature differences between the URT and LRT may play a role in the behavior of the virus and response to infection in these compartments. Furthermore, the poor conservation of ORF8 among related coronaviruses [61], the appearance of a 382 nucleotide deletion in the ORF8 of SARS-CoV-2 isolates in patients during February 2020 [62], and the circulation of a SARS-CoV-2 isolate containing a truncated version of ORF8 from March through October 2020 [63] suggest that ORF8 is a hotspot for SARS-CoV-2 adaptation and evolution. For example, the alpha variant, which we also characterized in our study, carries a stop codon at amino acid 27 of ORF8, resulting in the expression of a truncated ORF8 protein [64]. Interestingly, in our model, ΔORF8 and Alpha did not phenocopy in terms of URT replication, cytokine responses, or transmission. It is possible that alpha's truncated ORF8 retains functions that are critical for URT replication. Another possibility is that alpha's ORF8 is defunct, but that other viral proteins, some of which are different from the WA-1 background, provide redundant immune suppression mechanisms that compensate for the lack of ORF8 action in alpha. Future studies with additional recombinant SARS-CoV-2 will enable detangling the different hypotheses.

In conclusion, additional studies are needed to elucidate the role and mechanism of individual cytokines and viral accessory proteins, such as ORF8, in SARS-CoV-2 transmission. Our neonatal mouse model of SARS-CoV-2 transmission paves the way to such future

mechanistic studies, as it also enables the modulation of the host's immune responses by taking advantage of available transgenic mice with deletions in individual pathway components.

In summary, we established a SARS-CoV-2 transmission model using neonatal K18-hACE2 transgenic mice that characterizes the net effect of variant-inherent mutations on viral tropism and transmission and uncovers for the first time the contribution of accessory proteins to transmission. Using this tractable animal model to define the molecular mechanisms underlying SARS-CoV-2 transmission could guide the development of superior antiviral therapies and contribute to a greater understanding of not only SARS-CoV-2, but respiratory viruses in general.

Materials and Methods

Cell lines

Vero E6 cells were cultured in Dulbecco modified Eagle medium (DMEM) (Gibco) supplemented with 10% fetal bovine serum (FBS) (Atlanta Biologicals), 1% Penn/Strep (Gibco) and 1% Amphotericin B (Gibco) at 37°C with 5% CO2.

Vero E6-TMPRSS2-T2A-ACE2 cells were cultured in DMEM (Corning) containing 4 mM L-glutamine, 4500 mg per L glucose, 1 mM sodium pyruvate and 1500 mg per L sodium bicarbonate, supplemented with 10% fetal bovine serum and 10 µg per mL puromycin (Sigma) at 37°C with 5% CO_2. All cell lines were confirmed to be mycoplasma free.

Mice

C57BL/6J and K18-hACE2 C57BL/6J (strain 2B6.Cg-Tg(K18-ACE2)2Prlmn/J) mice (Jackson Laboratories, ME) were maintained and bred in a conventional animal facility. In order to produce neonatal heterozygous K18-hACE2 C57BL/6J mice for the transmission experiments, C57BL/6J females were bred with homozygous K18-hACE2 C57BL/6J males. Pups were housed with their mother for the duration of all experiments. Animal experiments were performed in the Animal Biosafety Level 3 (ABSL3) facility of NYU Grossman School of Medicine (New York, NY), in accordance with its Biosafety Manual and Standard Operating Procedures, and following Institutional Animal Care and Use Committee (IACUC) guidelines.

Biosafety and work with biohazardous material

All work with infectious SARS-CoV-2 isolates and recombinant viruses, including work with infected animals, was performed in the Animal Biosafety Level 3 (ABSL3) facilities of the University of Maryland (Baltimore, MD) and NYU Grossman School of Medicine (New York, NY). Both facilities are registered with their respective local Departments of Health and passed

inspections by the Centers for Disease Control & Prevention (CDC) within the year of submission of this manuscript. ABSL3 facilities are operated in accordance with their Biosafety Manuals and Standard Operating Procedures, including for the containment of biohazardous aerosols through the use of certified biosafety cabinets and the facilities' sealed ventilation systems that provide a sustained directional airflow, from clean towards potentially contaminated areas, and HEPA-filtered exhaust. Biohazardous waste generated in the facilities is fully decontaminated using approved disinfectants followed by autoclaving and incineration as Regulated Medical waste. Access to ABSL3 facilities is restricted to certified and authorized personnel, enrolled into occupational health surveillance programs, and wearing adequate Personal Protective Equipment (PPE), including OSHA-approved respirators, eye protection, spill-resistant coveralls and double-gloves. When analyzed outside of ABSL3 facilities, infectious samples were thoroughly treated using vetted inactivation methods.

All work with infectious SARS-CoV-2 isolates and recombinant viruses was performed with prior approval of the Institutional Biosafety Committees (IBCs) of the University of Maryland School of Medicine and NYU Grossman School of Medicine. Import permits for SARS-CoV-2 variant isolates were approved by the CDC. Generation of recombinant SARS-CoV-2 viruses was approved for M.F. by the IBC of the University of Maryland School of Medicine.

Generation of Virus Stocks

The following reagents were obtained through BEI Resources, NIAID, NIH: SARS-Related Coronavirus 2, Isolate USA-WA1/2020, NR-52281, deposited by the Centers for Disease Control and Prevention; SARS-Related Coronavirus 2, Isolate hCoV-19/England/204820464/2020, B.1.1.7, NR-54000, contributed by Bassam Hallis; SARS-Related Coronavirus 2, Isolate hCoV-19/South Africa/KRISP-K005325/2020, B.1.351, NR-54009, contributed by Alex Sigal and Tulio de Oliveira; SARS-Related Coronavirus 2, Isolate hCoV-19/Japan/TY7-503/2021 (Brazil P.1), NR-54982, contributed by National Institute of Infectious Diseases. SARS-CoV-2 Delta variant

466 (hCoV19/USA/PHC658/2021) and SARS-CoV-2 Omicron BA.1 (hCoV-19/USA/GA-EHC-
467 2811C/2021) were kindly provided by the Suthar Lab at Emory University. The USA-WA1/2020
468 stock was produced as previously described [65]. The other SARS-CoV-2 viruses were passaged
469 once in Vero E6 cells supplemented with 1 µg/ml of l-1-tosylamido-2-phenylethyl chloromethyl
470 ketone (TPCK)-trypsin, to avoid virus adaptation to Vero E6 cells due to the lack of TMPRSS2
471 expression. Cells were infected at an MOI of 0.01 and harvested at 50% cytopathic effect (CPE).
472 After harvest, virus was purified using a 25% sucrose cushion at 25,000 RPM for 3-4 hours and
473 resuspended using PBS prior to infection. For the B.1.1.7, B.1.1.351 and P.1, stocks, aliquots
474 were initially plaque-purified and sequenced to verify the variant signature before expanding in
475 the presence of TPCK-trypsin to generate a passage 1 working stock. WA-1 ΔORF6, WA-
476 1ΔORF8 and its WA-1 control were generated in the Frieman Lab at University of Maryland
477 School of Medicine[60]; aliquots were used as provided for the experiments. For heat-inactivated
478 (HI) SARS-CoV-2 WA-1, viral stocks were incubated at 56ºC for 5 hours. Samples were titered
479 for confirmation of complete inactivation of infectious particles.
480
481 Immunohistochemistry on mouse heads
482 Pups infected as described above were euthanized according to humane, IACUC-approved
483 procedure at 2 dpi. The skin of heads was gently removed to preserve nasal structures. Heads
484 were then removed and submerged in PBS at 4°C for a brief wash, followed by fixing in 4%
485 paraformaldehyde for 72 h at 4°C without shaking. Heads were then washed in PBS at 4°C with
486 gentle swirling for 20 min, followed by decalcification into 0.12M EDTA solution at 4°C with gentle
487 shaking for 7 days. Intact heads were then processed through graded ethanols to xylene and
488 infiltrated with paraffin in a Leica Peloris automated tissue processor. Paraffin-embedded sections
489 were immunostained on a Leica BondRX, according to manufacturer's instructions. In brief,
490 deparaffinized sections underwent a 20 minute heat retrieval in Leica ER2 buffer (pH9, AR9640)
491 followed by Rodent Block (Biocare, RBM961 L) prior to a one hour incubation with SARS-CoV-2

N protein antibody (clone 1C7C7) at a 1:300 dilution and a AF594-conjugated Goat-anti-mouse secondary (ThermoFisher, A11005). Slides were counterstained with DAPI and scanned on an Akoya Polaris Vectra imaging system. Images were viewed and prepared with Akoya Phenochart and OMERO software prior to exporting as TIF files.

Virus infection, shedding, and transmission.

Index pups in a litter (4 to 7 days of age) were infected with a 3 µL sterile PBS inoculum without general anesthesia (to avoid direct lung inoculation) by intranasal instillation of 30 PFU of SARS-CoV-2 WA-1, SARS-CoV-2 variant or recombinant SARS-CoV-2 and returned to the litter for the duration of the experiment. Shedding of virus was collected by dipping the nares of each mouse into viral medium (PBS plus 0.3% bovine serum albumin [BSA]) daily, and samples were evaluated via quantitative reverse transcription-PCR (RT-qPCR) or plaque assay. Intra-litter transmission was assessed by collecting shedding samples daily in the littermates (contact). The pups and mother were euthanized by CO_2 asphyxiation followed by cardiac puncture. The upper respiratory tract (URT) was subjected to a retrotracheal lavage (flushing of 300 µL PBS from the trachea and collecting through the nares), and samples were used to quantify virus (via plaque assay or qRT-PCR). Ratios of index to contact pups ranged from 1:6-9 for variant comparison to 1:3-1:4 for model optimization with WA-1.

Viral quantification RT-qPCR

RNA extractions were performed using the Qiagen QIAamp Viral RNA kit. The number of viral N copy number per uL was quantified by RT-qPCR using the Taqman® RNA-to-CT One-Step RT-PCR kit (Applied Biosystems™) with SARS-CoV-2 primers and probe targeting an amplicon in the N protein of SARS-CoV-2 WA-1 (Forward: 5'ATGCTGCAATCGTGCTACAA3'; reverse: 5' GACTGCCGCCTCTGCTC3') and the probe 5'/56-

FAM/TCAAGGAAC/ZEN/AACATTGCCAA/3IABkFQ/3'. A standard curve was generated for each dataset using in vitro transcribed SARS-CoV-2 N RNA sequence (MN985325.1).

Viral quantification

Infectious viral titers were determined by plaque assay. In brief, 10-fold dilutions of each virus in DMEM + 1% antibiotic/antimycotic (Gibco) were added to a monolayer of Vero E6 or Vero E6-TMPRSS2-T2A-ACE2 cells for 1 h at 37ºC. Following incubation, cells were overlaid with 0.8% agarose in DMEM containing 2% FBS and incubated at 37ºC for 36 hrs. Cells were fixed with 10% formalin, the agarose plug removed, and plaques visualized by crystal violet staining. Samples obtained from mouse experiments (shedding, lavage, and lung homogenates) were tittered in Vero E6-TMPRSS2-T2A-ACE2 to increase system sensitivity while stocks and inoculum for each transmission event were tittered in Vero E6.

Lung viral titer quantification

Lungs were collected in 500 µL of DPBS containing one stainless steel bead (QIAGEN), homogenized with the Tissue-Lyser II (QIAGEN), and debris were pulled down at 8000 rpm for 8 min. Viral titers were determined by plaque assay using Vero E6-TMPRSS2-T2A-ACE2 cells.

Cytokine and chemokine protein measurements

Cytokine and chemokine levels were measured in mouse serum using the Bio-Plex Pro Mouse Cytokine 23-plex Assay (Bio-Rad). Cytokines and chemokines were recorded on a MAGPIX machine (Luminex) and quantitated via comparison to a standard curve. xPONENT version 4.3.229.0 software was used for the data collection and analysis. Clustered heatmaps were generated using the ComplexHeatmap package in program R v.4.1.2 [66]

Quantification and statistical analysis

All statistical analyses were performed using GraphPad Prism. Each experiment was completed at least two independent times with internal biological duplicates unless otherwise noted in the figure legends. The exact number of biological replicates (n) can be found in the figure legends. Data are represented as the geometric mean ± geometric standard deviation (SD). Kruskal-Wallis, one-way ANOVA test with Bonferroni post hoc test and log-rank Mantel-Cox tests were performed and specifically indicated in the figure legends. Only p-values < 0.05 were displayed in the figures and p-values > 0.05 were considered non-significant (ns).

Acknowledgements:

We thank Thomas M. Moran, Icahn School of Medicine at Mount Sinai, and Luis Martínez-Sobrido, Texas Biomedical Institute, for the kind gift of mouse monoclonal SARS-CoV N antibody 1C7, and Mehul Suthar, Emory School of Medicine, for the gift of the variants. We are grateful to the SARS-CoV-2 Assessment of Viral Evolution Program for critical input on our data.

Histopathology of the murine nasopharynx was performed by Mark Alu, Branka Brukner Dabovic, and Cynthia Loomis from the NYUMC Experimental Pathology Research Laboratory (RRID: SCR_017928). Both the Experimental Pathology Research Laboratory and the NYU Genome Technology Core are supported by NYU Cancer Center support grant P30CA016087 and by NYU Langone's Laura and Isaac Perlmutter Cancer Center and the Vectra Polaris multispectral scanner was purchased through a Shared Instrument Grant S10 OD021747. We are also grateful to Adriana Heguy and team from the NYU Genome Technology Core for deep-sequencing of all viruses used in this study.

Research was partially supported by the following grants from NIH/NIAID: R01AI143639 to M.D., K08AI141759 to M.B.O, R01AI143861 and R01AI143861 to K.M.K., T32AI007180. None of the work with recombinant SARS-CoV-2 at NYU Grossman School of Medicine was funded by NIAID. Work was further supported by The Vilcek Institute of Graduate Biomedical Sciences, and by NYU Grossman School of Medicine Startup funds.

References

1 Richard, M. *et al.* SARS-CoV-2 is transmitted via contact and via the air between ferrets. *Nature Communications* **11**, 3496, doi:10.1038/s41467-020-17367-2 (2020).

2 Sia, S. F. *et al.* Pathogenesis and transmission of SARS-CoV-2 in golden hamsters. *Nature* **583**, 834-838, doi:10.1038/s41586-020-2342-5 (2020).

3 Pan, T. *et al.* Infection of wild-type mice by SARS-CoV-2 B.1.351 variant indicates a possible novel cross-species transmission route. *Signal Transduction and Targeted Therapy* **6**, 420, doi:10.1038/s41392-021-00848-1 (2021).

4 Callaway, E. What Omicron's BA.4 and BA.5 variants mean for the pandemic. *Nature* **606**, 848-849, doi:https://doi.org/10.1038/d41586-022-01730-y (2022).

5 Qu, P. *et al.* Evasion of Neutralizing Antibody Response by the SARS-CoV-2 BA.2.75 Variant. *bioRxiv*, doi:10.1101/2022.08.14.503921 (2022).

6 Kyriakidis, N. C., López-Cortés, A., González, E. V., Grimaldos, A. B. & Prado, E. O. SARS-CoV-2 vaccines strategies: a comprehensive review of phase 3 candidates. *npj Vaccines* **6**, 28, doi:10.1038/s41541-021-00292-w (2021).

7 Li, J.-Y. *et al.* The ORF6, ORF8 and nucleocapsid proteins of SARS-CoV-2 inhibit type I interferon signaling pathway. *Virus Research* **286**, 198074, doi:https://doi.org/10.1016/j.virusres.2020.198074 (2020).

8 Yuen, C.-K. *et al.* SARS-CoV-2 nsp13, nsp14, nsp15 and orf6 function as potent interferon antagonists. *Emerging Microbes & Infections* **9**, 1418-1428, doi:10.1080/22221751.2020.1780953 (2020).

9 Konno, Y. *et al.* SARS-CoV-2 ORF3b Is a Potent Interferon Antagonist Whose Activity Is Increased by a Naturally Occurring Elongation Variant. *Cell Rep* **32**, 108185, doi:10.1016/j.celrep.2020.108185 (2020).

10 Miorin, L. *et al.* SARS-CoV-2 Orf6 hijacks Nup98 to block STAT nuclear import and antagonize interferon signaling. *Proc Natl Acad Sci U S A* **117**, 28344-28354, doi:10.1073/pnas.2016650117 (2020).

11 Shemesh, M. *et al.* SARS-CoV-2 suppresses IFNβ production mediated by NSP1, 5, 6, 15, ORF6 and ORF7b but does not suppress the effects of added

interferon. *PLOS Pathogens* **17**, e1009800, doi:10.1371/journal.ppat.1009800 (2021).

12 Kopecky-Bromberg, S. A., Martínez-Sobrido, L., Frieman, M., Baric, R. A. & Palese, P. Severe acute respiratory syndrome coronavirus open reading frame (ORF) 3b, ORF 6, and nucleocapsid proteins function as interferon antagonists. *J Virol* **81**, 548-557, doi:10.1128/jvi.01782-06 (2007).

13 Frieman, M. *et al.* Severe Acute Respiratory Syndrome Coronavirus ORF6 Antagonizes STAT1 Function by Sequestering Nuclear Import Factors on the Rough Endoplasmic Reticulum/Golgi Membrane. *Journal of Virology* **81**, 9812-9824, doi:doi:10.1128/JVI.01012-07 (2007).

14 Schroeder, S. *et al.* Interferon antagonism by SARS-CoV-2: a functional study using reverse genetics. *Lancet Microbe* **2**, e210-e218, doi:10.1016/s2666-5247(21)00027-6 (2021).

15 Dolgin, E. Coronavirus variant threatens global recovery. *Nat Africa* doi:https://doi.org/10.1038/d44148-021-00021-4 (2021).

16 Bayarri-Olmos, R. *et al.* The alpha/B.1.1.7 SARS-CoV-2 variant exhibits significantly higher affinity for ACE-2 and requires lower inoculation doses to cause disease in K18-hACE2 mice. *eLife* **10**, e70002, doi:10.7554/eLife.70002 (2021).

17 Meng, B. *et al.* Altered TMPRSS2 usage by SARS-CoV-2 Omicron impacts infectivity and fusogenicity. *Nature* **603**, 706-714, doi:10.1038/s41586-022-04474-x (2022).

18 Montagutelli, X. *et al.* The B1.351 and P.1 variants extend SARS-CoV-2 host range to mice. *bioRxiv*, 2021.2003.2018.436013, doi:10.1101/2021.03.18.436013 (2021).

19 Saito, A. *et al.* Enhanced fusogenicity and pathogenicity of SARS-CoV-2 Delta P681R mutation. *Nature* **602**, 300-306, doi:10.1038/s41586-021-04266-9 (2022).

20 Lubinski, B. *et al.* Functional evaluation of the P681H mutation on the proteolytic activation of the SARS-CoV-2 variant B.1.1.7 (Alpha) spike. *iScience* **25**, 103589, doi:10.1016/j.isci.2021.103589 (2022).

21 Nelson, G. *et al.* Molecular dynamic simulation reveals E484K mutation enhances spike RBD-ACE2 affinity and the combination of E484K, K417N and N501Y mutations (501Y.V2 variant) induces conformational change greater than N501Y mutant alone, potentially resulting in an escape mutant. *bioRxiv*, 2021.2001.2013.426558, doi:10.1101/2021.01.13.426558 (2021).

22 Han, P. *et al.* Receptor binding and complex structures of human ACE2 to spike RBD from omicron and delta SARS-CoV-2. *Cell* **185**, 630-640.e610, doi:10.1016/j.cell.2022.01.001 (2022).

23 Shuai, H. *et al.* Attenuated replication and pathogenicity of SARS-CoV-2 B.1.1.529 Omicron. *Nature* **603**, 693-699, doi:10.1038/s41586-022-04442-5 (2022).

24 Port, J. R. *et al.* Increased small particle aerosol transmission of B.1.1.7 compared with SARS-CoV-2 lineage A in vivo. *Nature Microbiology* **7**, 213-223, doi:10.1038/s41564-021-01047-y (2022).

25 Escalera, A. *et al.* Mutations in SARS-CoV-2 variants of concern link to increased spike cleavage and virus transmission. *Cell Host Microbe* **30**, 373-387.e377, doi:10.1016/j.chom.2022.01.006 (2022).

26 Liu, Y. *et al.* The N501Y spike substitution enhances SARS-CoV-2 infection and transmission. *Nature* **602**, 294-299, doi:10.1038/s41586-021-04245-0 (2022).

27 Abdelnabi, R. *et al.* The omicron (B.1.1.529) SARS-CoV-2 variant of concern does not readily infect Syrian hamsters. *Antiviral Res* **198**, 105253, doi:10.1016/j.antiviral.2022.105253 (2022).

28 O'Donnell, K. L. *et al.* Pathogenic and transcriptomic differences of emerging SARS-CoV-2 variants in the Syrian golden hamster model. *EBioMedicine* **73**, 103675, doi:https://doi.org/10.1016/j.ebiom.2021.103675 (2021).

29 Yuan, S. *et al.* Pathogenicity, transmissibility, and fitness of SARS-CoV-2 Omicron in Syrian hamsters. *Science* **377**, 428-433, doi:10.1126/science.abn8939 (2022).

30 McMahan, K. *et al.* Reduced pathogenicity of the SARS-CoV-2 omicron variant in hamsters. *Med (N Y)* **3**, 262-268.e264, doi:10.1016/j.medj.2022.03.004 (2022).

31 Horspool, A. M. *et al.* SARS-CoV-2 B.1.1.7 and B.1.351 variants of concern induce lethal disease in K18-hACE2 transgenic mice despite convalescent plasma therapy. *bioRxiv*, 2021.2005.2005.442784, doi:10.1101/2021.05.05.442784 (2021).

32 Zhou, B. *et al.* SARS-CoV-2 spike D614G change enhances replication and transmission. *Nature* **592**, 122-127, doi:10.1038/s41586-021-03361-1 (2021).

33 Munster, V. J. *et al.* Subtle differences in the pathogenicity of SARS-CoV-2 variants of concern B.1.1.7 and B.1.351 in rhesus macaques. *Sci Adv* **7**, eabj3627, doi:10.1126/sciadv.abj3627 (2021).

34 Rosenke, K. *et al.* UK B.1.1.7 (Alpha) variant exhibits increased respiratory replication and shedding in nonhuman primates. *Emerging Microbes & Infections* **10**, 2173-2182, doi:10.1080/22221751.2021.1997074 (2021).

35 Silvas, J. A. *et al.* Contribution of SARS-CoV-2 Accessory Proteins to Viral Pathogenicity in K18 Human ACE2 Transgenic Mice. *J Virol* **95**, e0040221, doi:10.1128/jvi.00402-21 (2021).

36 Johnson, B. A. *et al.* Loss of furin cleavage site attenuates SARS-CoV-2 pathogenesis. *Nature* **591**, 293-299, doi:10.1038/s41586-021-03237-4 (2021).

37 Halfmann, P. J. *et al.* SARS-CoV-2 Omicron virus causes attenuated disease in mice and hamsters. *Nature* **603**, 687-692, doi:10.1038/s41586-022-04441-6 (2022).

38 Hou, Y. J. *et al.* SARS-CoV-2 D614G variant exhibits efficient replication ex vivo and transmission in vivo. *Science* **370**, 1464-1468, doi:10.1126/science.abe8499 (2020).

39 Li, R. *et al.* Production of Genetically Engineered Golden Syrian Hamsters by Pronuclear Injection of the CRISPR/Cas9 Complex. *J Vis Exp*, doi:10.3791/56263 (2018).

40 Ortigoza, M. B. *et al.* An Infant Mouse Model of Influenza Virus Transmission Demonstrates the Role of Virus-Specific Shedding, Humoral Immunity, and Sialidase Expression by Colonizing Streptococcus pneumoniae. *mBio* **9**, e02359-02318, doi:doi:10.1128/mBio.02359-18 (2018).

41 Huang, H., Zhu, Y., Niu, Z., Zhou, L. & Sun, Q. SARS-CoV-2 N501Y variants of concern and their potential transmission by mouse. *Cell Death & Differentiation* **28**, 2840-2842, doi:10.1038/s41418-021-00846-4 (2021).

42 McCray, P. B. *et al.* Lethal Infection of K18-hACE2 Mice Infected with Severe Acute Respiratory Syndrome Coronavirus. *Journal of Virology* **81**, 813-821, doi:doi:10.1128/JVI.02012-06 (2007).

43 Puhach, O. *et al.* Infectious viral load in unvaccinated and vaccinated individuals infected with ancestral, Delta or Omicron SARS-CoV-2. *Nature Medicine* **28**, 1491-1500, doi:10.1038/s41591-022-01816-0 (2022).

44 von Wintersdorff, C. J. H. *et al.* Infections with the SARS-CoV-2 Delta variant exhibit fourfold increased viral loads in the upper airways compared to Alpha or non-variants of concern. *Scientific Reports* **12**, 13922, doi:10.1038/s41598-022-18279-5 (2022).

45 Leung, N. H. L. Transmissibility and transmission of respiratory viruses. *Nature Reviews Microbiology* **19**, 528-545, doi:10.1038/s41579-021-00535-6 (2021).

46 Mostaghimi, D., Valdez, C. N., Larson, H. T., Kalinich, C. C. & Iwasaki, A. Prevention of host-to-host transmission by SARS-CoV-2 vaccines. *Lancet Infect Dis* **22**, e52-e58, doi:10.1016/s1473-3099(21)00472-2 (2022).

47 Zafar, M. A. *et al.* Identification of Pneumococcal Factors Affecting Pneumococcal Shedding Shows that the dlt Locus Promotes Inflammation and Transmission. *mBio* **10**, e01032-01019, doi:doi:10.1128/mBio.01032-19 (2019).

48 Zangari, T., Ortigoza Mila, B., Lokken-Toyli Kristen, L. & Weiser Jeffrey, N. Type I Interferon Signaling Is a Common Factor Driving Streptococcus pneumoniae and Influenza A Virus Shedding and Transmission. *mBio* **12**, e03589-03520, doi:10.1128/mBio.03589-20 (2021).

49 Lee, J.-G. *et al.* Characterization of SARS-CoV-2 proteins reveals Orf6 pathogenicity, subcellular localization, host interactions and attenuation by Selinexor. *Cell & Bioscience* **11**, 58, doi:10.1186/s13578-021-00568-7 (2021).

50 Winkler, E. S. *et al.* SARS-CoV-2 infection of human ACE2-transgenic mice causes severe lung inflammation and impaired function. *Nature Immunology* **21**, 1327-1335, doi:10.1038/s41590-020-0778-2 (2020).

51 Zhang, Y. *et al.* SARS-CoV-2 Rapidly Adapts in Aged BALB/c Mice and Induces Typical Pneumonia. *Journal of Virology* **95**, e02477-02420, doi:doi:10.1128/JVI.02477-20 (2021).

52 Yasui, F. *et al.* Infection with the SARS-CoV-2 B.1.351 variant is lethal in aged BALB/c mice. *Scientific Reports* **12**, 4150, doi:10.1038/s41598-022-08104-4 (2022).

53 Port, J. R. *et al.* Host and viral determinants of airborne transmission of SARS-CoV-2 in the Syrian hamster. *bioRxiv*, doi:10.1101/2022.08.15.504010 (2022).

54 Wibmer, C. K. *et al.* SARS-CoV-2 501Y.V2 escapes neutralization by South African COVID-19 donor plasma. *Nature Medicine* **27**, 622-625, doi:10.1038/s41591-021-01285-x (2021).

55 Planas, D. *et al.* Reduced sensitivity of SARS-CoV-2 variant Delta to antibody neutralization. *Nature* **596**, 276-280, doi:10.1038/s41586-021-03777-9 (2021).

56 Hoffmann, M. *et al.* The Omicron variant is highly resistant against antibody-mediated neutralization: Implications for control of the COVID-19 pandemic. *Cell* **185**, 447-456.e411, doi:10.1016/j.cell.2021.12.032 (2022).

57 Wu, X. *et al.* Viral Mimicry of Interleukin-17A by SARS-CoV-2 ORF8. *mBio* **13**, e0040222, doi:10.1128/mbio.00402-22 (2022).

58 Zhang, Y. *et al.* The ORF8 protein of SARS-CoV-2 mediates immune evasion through down-regulating MHC-I. *Proceedings of the National Academy of Sciences* **118**, e2024202118, doi:10.1073/pnas.2024202118 (2021).

59 Kee, J. *et al.* SARS-CoV-2 disrupts host epigenetic regulation via histone mimicry. *Nature* **610**, 381-388, doi:10.1038/s41586-022-05282-z (2022).

60 McGrath, M. E. *et al.* SARS-CoV-2 Variant Spike and accessory gene mutations alter pathogenesis. *bioRxiv*, doi:10.1101/2022.05.31.494211 (2022).

61 Pereira, F. Evolutionary dynamics of the SARS-CoV-2 ORF8 accessory gene. *Infect Genet Evol* **85**, 104525, doi:10.1016/j.meegid.2020.104525 (2020).

62 Young, B. E. *et al.* Effects of a major deletion in the SARS-CoV-2 genome on the severity of infection and the inflammatory response: an observational cohort study. *Lancet* **396**, 603-611, doi:10.1016/s0140-6736(20)31757-8 (2020).

63 DeRonde, S., Deuling, H., Parker, J. & Chen, J. Identification of a novel SARS-CoV-2 variant with a truncated protein in ORF8 gene by next generation sequencing. *Scientific Reports* **12**, 4631, doi:10.1038/s41598-022-08780-2 (2022).

64 Al-Rashedi, N. A. M. *et al.* High prevalence of an alpha variant lineage with a premature stop codon in ORF7a in Iraq, winter 2020-2021. *PLoS One* **17**, e0267295, doi:10.1371/journal.pone.0267295 (2022).

65 Vries, M. d. *et al.* A Comparative Analysis of SARS-CoV-2 Antivirals Characterizes 3CL^{pro} Inhibitor PF-00835231 as a Potential New Treatment for COVID-19. *Journal of Virology* **95**, e01819-01820, doi:doi:10.1128/JVI.01819-20 (2021).

66 R: A language and environment for statistical computing. R Foundation for Statistical Computing (Vienna, Austria, 2022).

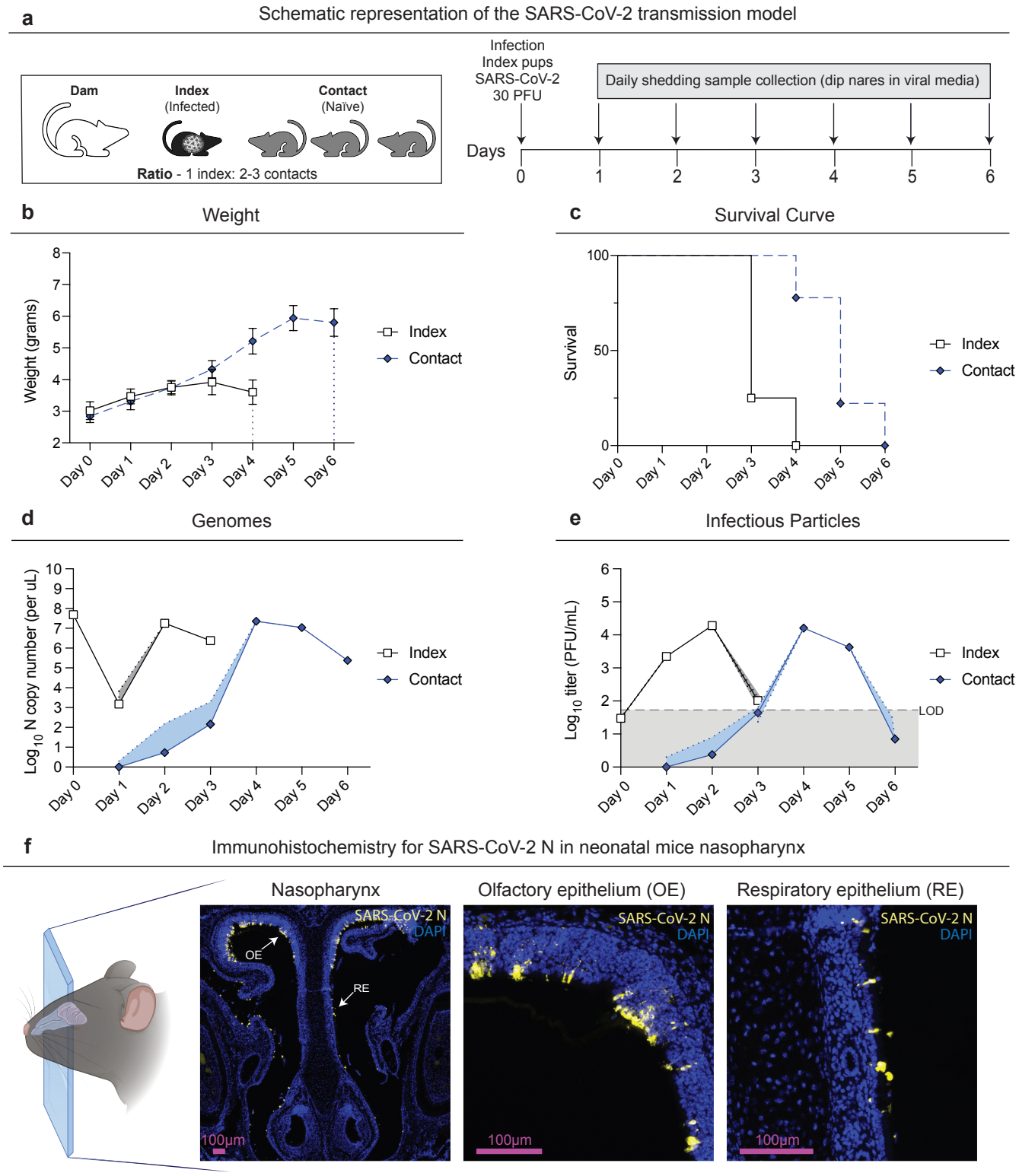

Figure 1. Establishment of a neonatal K18-hACE2 mouse transmission model. a, Schematic representation of the SARS-CoV-2 transmission model. At day 0 (4 to 7 days of age), K18-hACE2$^{+/-}$ pups were infected i.n. with 30 PFU of SARS-CoV-2 WA-1 (index) and cohoused with uninfected littermates (contact) for 6 days. Shedding of SARS-CoV-2 was collected by dipping the nares of each mouse in viral medium daily. **b**, Average body weight curve of index and contact mice infected with SARS-CoV-2 WA-1. Error bars indicate SEM. Dotted lines represent last day of survival of each group. **c**, Survival curve of index and contact mice after index infection with SARS-CoV-2 WA-1. **d,e** Viral burden in the shedding samples from were analyzed by RT-qPCR for viral RNA levels (**d**) and by plaque assay for infectious virus (**e**) Line and symbols represent the geometric mean and shaded area corresponds to the geometric standard deviation. Index and contact pups are shown by open or closed blue symbols, respectively. Data represents at least 2 independent repetitions. n = 4 - 6 contact mice per repetition. **f**, Immunohistochemistry for SARS-CoV-2 N in neonatal mice nasopharynx. At days 4-7 of age, pups were infected intranasally with 30 PFU of SARS-CoV-2 WA-1 and placed back with their mother for 2 days prior to sacrifice. Heads were fixed, paraffin embedded, sectioned through the nasopharynx, and stained for SARS-CoV-2 N protein (yellow) and DAPI (blue) for nuclei. Arrows represent areas magnified in the adjacent panels. OE - olfactory epithelium, RE - respiratory epithelium LOD - limit of detection

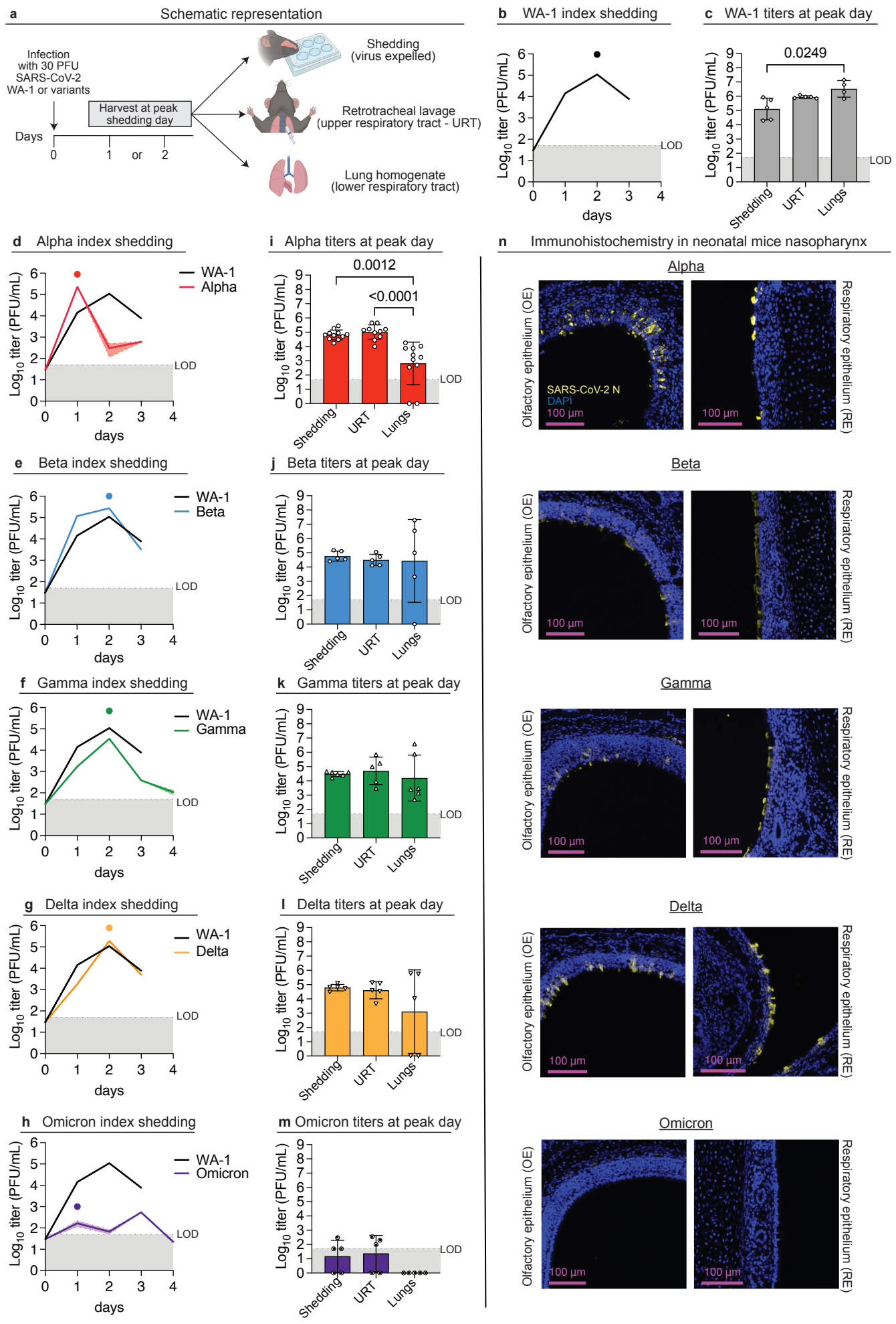

Figure 2: SARS-CoV-2 variant replication dynamics and tropism in index mice. a, Schematic representation of the experiment. At day 0 (4 to 7 days of age), K18-hACE2$^{+/-}$ pups were infected i.n. with 30 PFU of either SARS-CoV-2 WA-1 or the variants of concern alpha, beta, gamma, delta or omicron, collected shedding samples at days 1 and 2 and determined the peak day of viral shedding for each variant. At their peak day of viral shedding, we performed a retrotracheal lavage for the upper respiratory tract, and collected lung homogenate for the lower respiratory tract to quantify the amount of infectious virus via plaque assay. **b,d-h** Index mice shedding titers of mice infected with (**b**) WA-1, (**d**) alpha, (**e**) beta, (**f**) gamma, (**g**) delta or (**h**) omicron. Line represents the geometric mean and shaded area corresponds to the geometric standard deviation. Dot shows the first peak day of shedding. Data represents at least 2 independent repetitions with n = 6 - 15 index per group. Shaded gray area represents values below detection level. **c, i-m**. Viral titers of mice infected with either (**c**) WA-1, (**i**) alpha, (**j**) beta, (**k**) gamma, (**l**) delta or (**m**) omicron in different compartments. Each symbol represents the shedding titer measured from a single mouse while bars and error bars represent geometric mean and geometric standard deviation, respectively. Numbers represent p-values of Kruskal-Wallis test. **n**, Immunohistochemistry for SARS-CoV-2 N in neonatal mice nasopharynx infected with alpha, beta, gamma, delta or omicron variants. At days 4-7 of age, pups were infected intranasally with 30 PFU of the SARS-CoV-2 variants and placed back with their mother for 2 days prior to sacrifice. Heads were fixed, paraffin embedded, sectioned through the nasopharynx, and stained for SARS-CoV-2 N protein (yellow) and DAPI (blue) for nuclei. LOD - limit of detection

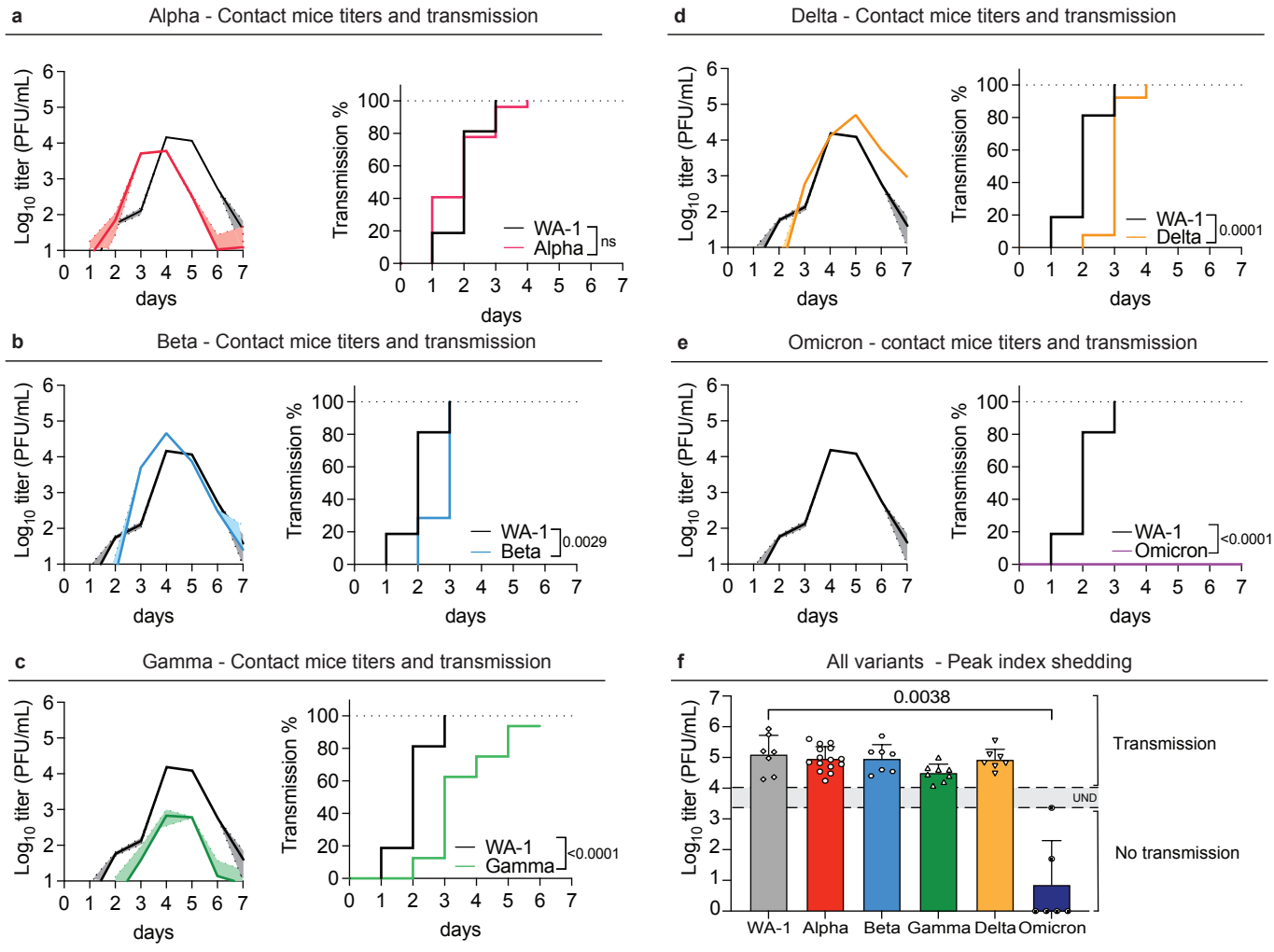

Figure 3: SARS-CoV-2 neonatal model reveals variant transmission dynamics. **a-e**, Left panel: Contact mice titers. Right panel: transmission curves for experiments performed with (**a**) alpha, (**b**) beta, (**c**) gamma, (**d**) delta or (**e**) omicron variants. At day 0 (4 to 7 days of age), K18-hACE2$^{+/-}$ pups were infected i.n. with 30 PFU of SARS-CoV-2 variants (index) and cohoused with uninfected littermates (contact) for 7 days at a ratio of 1 index to 6-9 contacts. Shedding of SARS-CoV-2 was collected by dipping the nares of each mouse in viral medium daily. Viral burden in the shedding samples of contact mice were analyzed by plaque assay for infectious virus. Line represent the geometric mean and shaded area corresponds to the geometric standard deviation. Transmission experiments with WA-1 are represented in black as a control. Data represents at least 2 independent repetitions with n = 2-4 index and n = 6-9 contacts per group. Numbers in the transmission curves represent p-values of Mantel-Cox Log-rank test. **d**, Peak index shedding titers of mice infected with SARS-CoV-2 variants. Each symbol represents the shedding titer measured from a single mouse while bars and error bars represent geometric mean and geometric standard deviation, respectively. Numbers represent p-values of Kruskal-Wallis test. Only significant values are presented. ns: not significant. UND: undertermined.

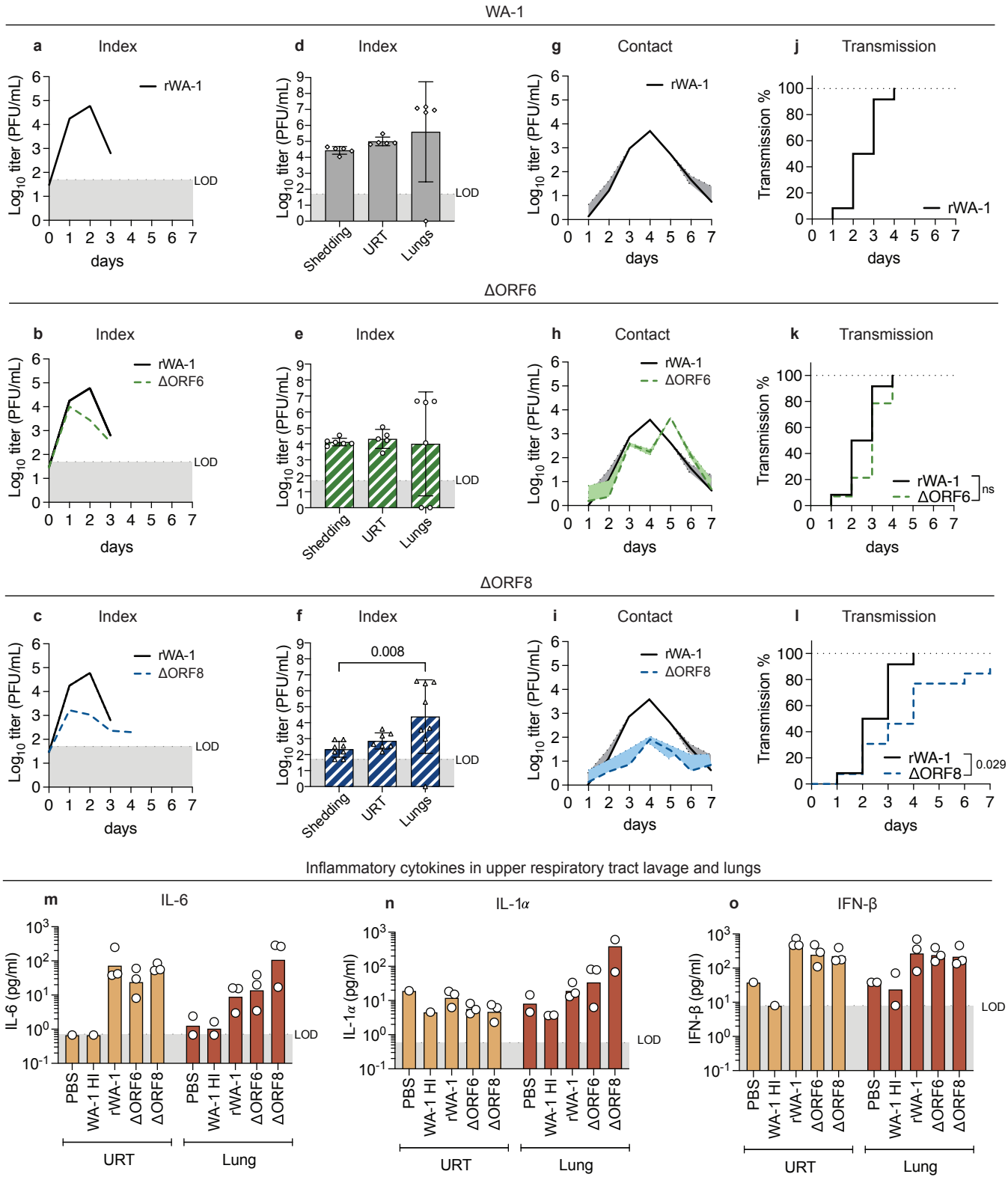

Figure 4. Characterization of replication and transmission of ΔORF6 and ΔORF8 viruses. a-c, Index mice shedding titers of mice infected with (**a**) recombinant WA-1 (rWA-1), (**b**) WA-1 lacking ORF6 (ΔORF6) or (**c**) WA-1 lacking ORF8 (ΔORF8). Line represents the geometric mean and shaded area corresponds to the geometric standard deviation. Dot shows the first peak day of shedding. Data represents at least 2 independent repetitions with n = 2-3 index per group. **d-f**, Viral titers of mice infected with either (**d**) rWA-1, (**e**) Δ ORF6, or (**f**) ΔORF8. in different compartments at 2dpi. Each symbol represents the shedding titer measured from a single mouse while bars and error bars represent geometric mean and geometric standard deviation, respectively. Numbers represent p-values of Kruskal-Wallis test. Only significant values are presented.n = 4-8 mice per group. **g-i**, Contact mice titers for transmission experiments performed with (**g**) rWA-1, (**h**) ΔORF6 or (**i**) ΔORF8. Viral burden in the shedding samples of contact mice were analyzed by plaque assay for infectious virus. Line represent the geometric mean and shaded area corresponds to the geometric standard deviation. Data represents at least 2 independent repetitions with n = 2-3 index and n = 6-9 contacts per group. **j-l**, Transmission curves for transmission experiments performed with (**j**) rWA-1, (**k**) ΔORF6 or (**l**) ΔORF8. Numbers represent p-values of Mantel-Cox Log-rank test. **m-o**, Inflammatory cytokine levels in the upper respiratory tract lavage or lungs of mice infected with either mock (PBS), heat-inactivated WA-1 (WA-1 HI), rWA-1, ΔORF6 or ΔORF8. Shaded gray area representes values below the detection level. LOD = limit of detection. URT = upper respiratory tract lavage